nature photonics
LETTERS
https://doi.org/10.1038/s41566-019-0349-y

# Electron–hole liquid in a van der Waals heterostructure photocell at room temperature

Trevor B. Arp [1,2,5], Dennis Pleskot [2,3,5], Vivek Aji [1] and Nathaniel M. Gabor [1,2,3,4]*

**In semiconductors, photo-excited charge carriers exist as a gas of electrons and holes, bound electron–hole pairs (excitons), biexcitons and trions[1–4]. At sufficiently high densities, the non-equilibrium system of electrons ($e^-$) and holes ($h^+$) may merge into an electronic liquid droplet[5–10]. Here, we report on the electron–hole liquid in ultrathin $MoTe_2$ photocells revealed through multi-parameter dynamic photoresponse microscopy (MPDPM). By combining rich visualization with comprehensive analysis of very large data sets acquired through MPDPM, we find that ultrafast laser excitation at a graphene–$MoTe_2$–graphene interface leads to the abrupt formation of ring-like spatial patterns in the photocurrent response as a function of increasing optical power at $T = 297$ K. The sudden onset to these patterns, together with extreme sublinear power dependence and picosecond-scale photocurrent dynamics, provide strong evidence for the formation of a two-dimensional electron–hole liquid droplet. The electron–hole liquid, which features a macroscopic population of correlated electrons and holes, may offer a path to room-temperature optoelectronic devices that harness collective electronic phenomena.**

Ultrathin $MoTe_2$ is an ideal semiconductor for the study of collective electron–hole phases, yet no measurements on two-dimensional (2D) transition metal dichalcogenides (TMDs) have shown evidence for the gas-to-liquid phase transition. Very high electron–hole densities have been demonstrated in TMDs using ultrashort laser pulses, giving rise to giant bandgap renormalization[11,12] and strong exciton–exciton interactions[13,14]. By integrating multi-layer $MoTe_2$ into graphene–$MoTe_2$–graphene van der Waals (vdW) heterostructures, such strong many-body effects may be accessed in the ultrasensitive near-infrared optoelectronic response[15–18], which results from the ~1 eV indirect bandgap and long exciton lifetimes[19–21]. As vdW heterostructure photocell device complexity increases, however, efficient photoresponse techniques must be developed to observe, manipulate and harness novel 2D electronic phases.

By incorporating ultrafast optoelectronic measurements[22–27] with efficient data acquisition, automation and analysis, we rapidly and densely sample a broad optoelectronic parameter space using a technique called multi-parameter dynamic photoresponse microscopy (MPDPM) (details in Supplementary Section 1). MPDPM uses a near-infrared ultrafast laser, in which ultrashort (150 fs) laser pulses are split into two distinct paths. A translation stage controls the path length difference between the split pulses. The two identical-power beams are then recombined and the path length difference of the delayed beam results in a time delay between pulses $\Delta t$ (Fig. 1a). The recombined beam is focused to a diffraction-limited spot that is spatially scanned across the 2D optoelectronic devices under high vacuum (Supplementary Section 1.1). The laser-induced photocurrent generated across a graphene–$MoTe_2$–graphene photocell (Fig. 1a) is measured at each point in space, resulting in a map of the interlayer photocurrent response (Fig. 1b) (see Methods).

Using dynamic photoresponse microscopy, we acquire a multi-dimensional data set of interlayer photocurrent $I$ versus two spatial dimensions, laser power $P$, time delay $\Delta t$ and interlayer voltage $V_i$ (Supplementary Section 1.3). This imaging process is repeated as a function of increasing optical power (Supplementary Video 1), while incrementing $\Delta t$ and $V_i$. Figure 1c shows that the interlayer photocurrent increases sub-linearly with increasing power at $\Delta t = 50$ ps under high vacuum. Such a photoresponse is consistent with previous photocurrent measurements of TMD photocells[15,16,26,27]: photogenerated electron–hole pairs are promoted across the indirect bandgap of $MoTe_2$ and collected as individual electrons and holes (Fig. 1c inset).

Our data-intensive technique allows us to gain a comprehensive understanding of the ordinary $MoTe_2$ heterostructure photoresponse. The photocurrent power dependence (Fig. 1c) is described well by a single power law, $I \propto P^{\gamma}$, where the power law exponent $\gamma = 0.44$ parameterizes the nonlinearity of the photoresponse. A power law exponent $\gamma \sim 1/2$ suggests straightforward dynamics with a simple rate equation $\mathrm{d}N/\mathrm{d}t = -N/\tau_{\mathrm{esc}} - \alpha N^2$, where $N$ is the electron–hole pair density, $\tau_{\mathrm{esc}}$ is the carrier escape time and $\alpha$ is the exciton–exciton annihilation rate[25] (Supplementary Section 4). By including a constant generation rate, the steady state ($\mathrm{d}N/\mathrm{d}t = 0$) solution to this rate equation results in a photocurrent $I \propto P^{1/2}$, in good agreement with the observed $I \propto P^{0.44}$. However, since MPDPM uses ultrashort pulses, careful time integration of the dynamics is required, resulting in an analytic solution $I \propto \ln(1 + N_0 \alpha \tau_{\mathrm{esc}})/\alpha \tau_{\mathrm{esc}}$, where $N_0$ is the electron–hole density immediately following the laser pulse (Supplementary Section 4.1). The analytic solution (red dashed line Fig. 1c) exhibits excellent agreement with the photocurrent data (blue data) and the power law fit (blue line). We conclude that $\gamma$ is thus a robust parameterization of the nonlinear photoresponse.

The multi-parameter dynamic photoresponse microscope visualizes the nonlinear photoresponse with extraordinary spatio-temporal detail (Fig. 1d–h). From a large set of photocurrent images (as in Fig. 1b), the interlayer photocurrent versus optical power is fitted to $I \propto P^{\gamma}$ at each point in space. This large data set is condensed into an image of the photocurrent nonlinearity $\gamma$ $(x,y)$, which we then measure as a function of $\Delta t$ (Supplementary Video 2). A snapshot from the spatio-temporal dynamics at $\Delta t = 120$ ps (Fig. 1d) shows that the nonlinearity $\gamma$ $(x,y)$ is nearly uniform over the active area

---

[1] Department of Physics and Astronomy, University of California, Riverside, Riverside, CA, USA. [2] Laboratory of Quantum Materials Optoelectronics, University of California, Riverside, Riverside, CA, USA. [3] Department of Materials Science and Engineering, University of California, Riverside, Riverside, CA, USA. [4] Canadian Institute for Advanced Research, Toronto, Ontario, Canada. [5] These authors contributed equally: Trevor B. Arp, Dennis Pleskot. *e-mail: nathaniel.gabor@ucr.edu

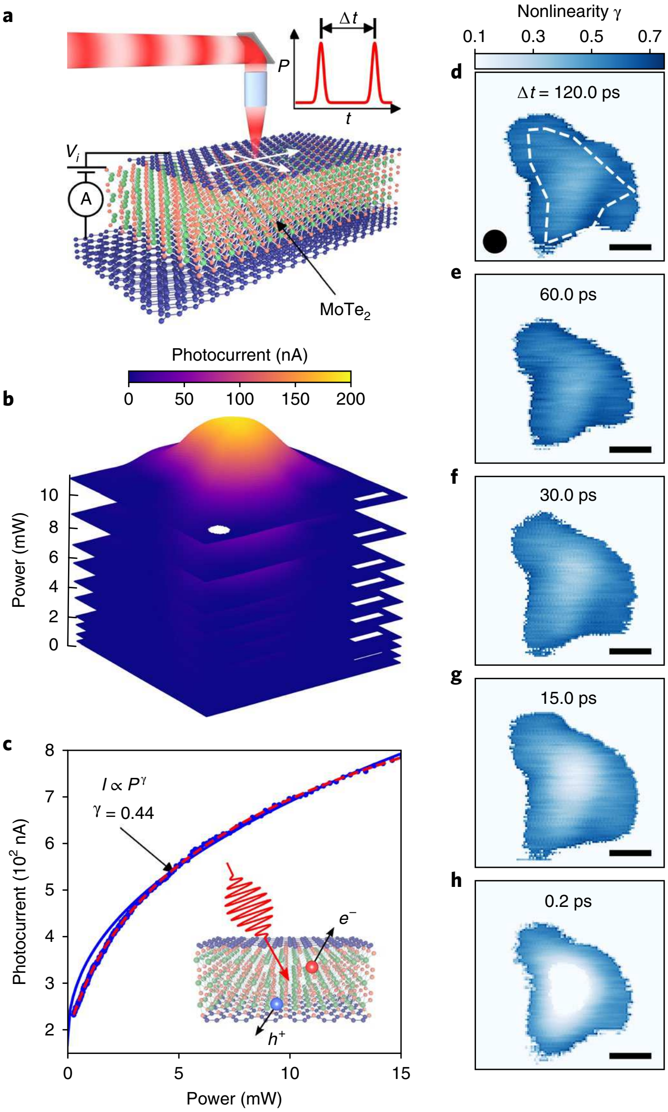

**Fig. 1 | Multi-parameter dynamic photoresponse microscopy (MPDPM) of ultrathin MoTe$_2$ photocells.** **a**, Schematic of the photocell and measurement. **b,** MPDPM images for increasing laser power; wavelength $\lambda = 1{,}200$ nm, $T = 297$ K and time delay $\Delta t = 120$ ps. **c**, Photocurrent versus optical power in the centre of the heterostructure (blue data) of thickness 9 nm. The solid blue line is a fit to a power law and the red dashed line is the analytical model fit. Inset, schematic of photoexcitation and collection of electrons ($e^-$) and holes ($h^+$) in MoTe$_2$. **d–h**, MPDPM images of the power law exponent, $\gamma(x,y)$, as a function of two-pulse time delay $\Delta t$ (labelled). The dashed line in **d** outlines the graphene–MoTe$_2$–graphene heterostructure. Scale bars 3 μm. Circles indicate the FWHM of the diffraction-limited beam spot.

of the MoTe$_2$ heterostructure (dashed outline Fig. 1d), exhibiting a narrow range $\gamma = 0.45$–$0.60$. The spatially uniform photoresponse with $I \propto P^{1/2}$ at long time delay is fully consistent with the ordinary photoresponse due to exciton–exciton interactions[13,14,25] (see Supplementary Section 4 for a detailed discussion).

Strikingly, when the time delay between laser pulses is very short, MPDPM reveals a highly anomalous photoresponse. At $\Delta t = 0.2$ ps (Fig. 1h), the power law behaviour collapses near the centre, resulting in a pronounced ring of sublinear photoresponse ($\gamma \sim 0.5$). Figure 1f,g shows that the sudden collapse near $\Delta t = 0.2$ ps is preceded by a gradual suppression of $\gamma$ at longer time delays. The area of power law suppression significantly exceeds the beam spot size, indicating a global change in photoresponse. This behaviour is not a permanent change of device response. Instead, we observe $\gamma$ suppression only at short time delay, whereas the ordinary photoresponse is recovered as soon as the laser intensity is reduced. In the following, we examine the space–time evolution of the MoTe$_2$ photoresponse, and extract the detailed dependence of the spatial photocurrent features on optical power, interlayer voltage and time delay.

We first decompose the MPDPM image measured at $\Delta t = 0.2$ ps (Fig. 1h) and examine the constituent photocurrent maps (Fig. 2). At low optical powers, the photocurrent magnitude increases rapidly and monotonically (Fig. 2a). For $P > 5$ mW, however, the photocurrent at the centre of the device suddenly decreases, forming a photocurrent ring of bright photoresponse (see Supplementary Video 3). The photocurrent ring grows rapidly with increasing optical power. To see the ring expansion more clearly, Fig. 2b shows the magnitude of the spatial gradient of the photocurrent maps $|\nabla I|$, which we use to visualize the local slope of the spatially resolved photocurrent landscape. At an optical power $P = 5$ mW, a clear edge begins to emerge and grows into a well-formed ring.

Remarkably, the anomalous photocurrent ring appears abruptly with increasing optical power. Using the gradient maps (Fig. 2b), we quantify the ring area by algorithmically identifying the contour $|\nabla I| \approx 0$ (see Supplementary Section 1.5 for details). Figure 2c shows the power dependence of the ring volume (product of area and sample thickness) as a fraction of the total heterostructure volume. At a critical power $P_C = 5$ mW, we observed a nearly discontinuous growth rate of the volume fraction. Above the transition $P > P_C$, the photocurrent ring, and thus volume fraction, expands linearly with optical power.

The sharp transition at $P_C$ also manifests as a sudden deviation from power law behaviour. Figure 2c (lower right inset) shows the spatially integrated photocurrent versus power measured along the dashed line in Fig. 2a. The photocurrent increases rapidly at low power and exhibits ordinary power law growth (solid green line Fig. 2c, lower right inset). Above $P = P_C$, however, the data falls significantly below the power law fit, and the spatially integrated photocurrent remains nearly constant as power increases. Thus, the abrupt formation and expansion of the photocurrent ring corresponds directly to the collapse of power law behaviour observed in Fig. 1h. For $\Delta t > 0.2$ ps the same behaviour occurs at higher $P_C$ (as shown in Supplementary Section 3.2) since the pulses become separated in time and the effect of each individual pulse is weaker than when they are combined.

The anomalous photoresponse at room temperature is reminiscent of the gas-to-liquid phase transition of electron–hole pairs in conventional semiconductors—such as Si, Ge, GaAs and CdS—at low temperatures[6,7,10]. At low laser power, photo-excitation generates a gas of electrons and holes (Fig. 3a). Enhanced Coulomb interactions bind electrons and holes into excitons with a nanometre-scale Bohr radius $a_B$[5–7,10]. The electron–hole pair density increases with laser power until exciton–exciton interactions become comparable to interactions within an individual bound electron–hole pair. Below the power threshold for the phase transition $P_C$, ordinary two-body ($N^2$) exciton–exciton annihilation processes dominate the optoelectronic properties.

At the critical laser power $P_C$, the electron–hole population merges into a non-equilibrium many-body phase (Fig. 3a). The electron–hole pair density $N$ becomes so large that the average spacing between pairs is nearly equal to the exciton radius (Fig. 2c, upper left inset). At $P_C = 5$ mW, the mean exciton–exciton separation, which we estimate to be $a_{xx} = 1$–$3$ nm in MoTe$_2$ (Supplementary Section 5.1), is very close to the Bohr radius $a_B = 2.3$ nm extracted from magneto-optical measurements[28]. Once $a_{xx} \sim a_B$, the electron–hole population reaches the critical density $N_C \sim 0.5\ \text{nm}^{-3}$ electron–hole pairs.

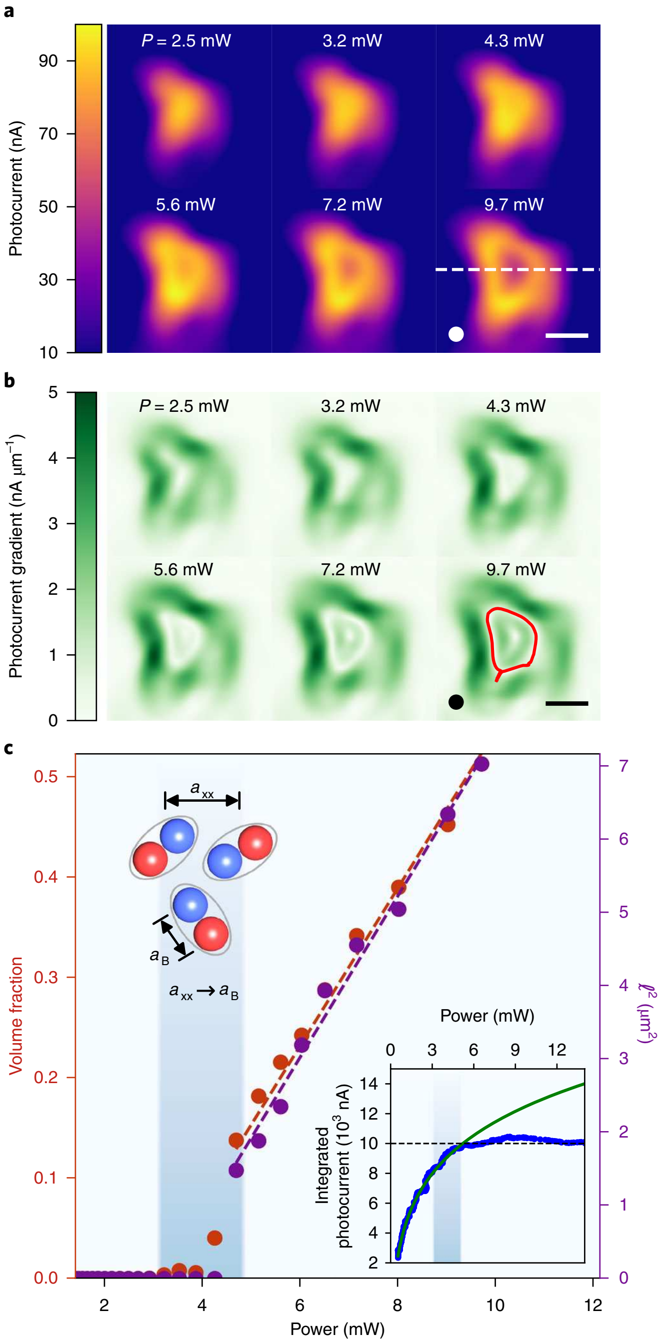

**Fig. 2 | Critical onset of ring-like photoresponse revealed through MPDPM.** **a**, Spatially resolved photocurrent versus power (labelled), $\Delta t = 0.2$ ps. The dashed line indicates the location of the photocurrent line profiles. **b**, Photocurrent gradient $|\nabla I|$ calculated from photocurrent maps in **a**. The contour $|\nabla I| \approx 0$ encloses the photocurrent ring (red contour in the image at $P = 9.7$ mW). Scale bars 5 µm, circles indicate FWHM of the beamspot. **c**, Photocurrent ring volume fraction (red data) versus laser power. The volume fraction is the ratio of the volume enclosed by the $|\nabla I| \approx 0$ contours to the active photocell volume (area). Peak-to-valley distance $\ell$ (purple data) versus power extracted from line cuts in **a**. Red (purple) dashed lines are linear fits to volume fraction ($\ell^2$) versus power above $P_C$. Top inset, inter-exciton spacing $a_{xx}$ approaches the exciton Bohr radius $a_B$. Bottom inset, spatially integrated photocurrent versus power (blue data) and power law fit below $P_C$ (solid green line).

This density $N_C$, which is determined by the renormalized minimum energy per electron–hole pair (Supplementary Fig. 14), remains constant in the liquid phase. Above the phase transition, the renormalization of the energy per electron–hole pair results in a suppression of photon absorption within the electron–hole liquid[11,12]. The resulting electron–hole liquid exhibits a fixed electron–hole pair density $N_C$, is highly polarizable in an applied electric field, and forms a sharp, stable boundary that separates it from the gas phase[5–7]. Electrons and holes in the liquid phase move independently from another within the confined liquid volume, yet they are not able to escape without sufficient excess energy.

We attribute the anomalous photoresponse in graphene–$MoTe_2$–graphene photocells to an electron–hole liquid phase, the properties of which are readily revealed through MPDPM. First, the liquid phase is characterized by a highly unusual ring-like interlayer photoresponse, which results from the fast interlayer transit of liberated electrons and holes near the edge of the droplet. At the surface of the photocell device, the excitation laser forms a diffraction-limited Gaussian beam spot with a full-width at half-maximum (FWHM) of 1.67 µm. When the local maximum power of the Gaussian beam exceeds the critical power threshold $P_C$, an electron–hole liquid droplet forms near the centre of the beam spot. The observed photocurrent results from electrons and holes at the edges of the electron–hole liquid. The characteristic ring shape then arises from the convolution of the beam spot with a sharply bound region of suppressed absorption (see Materials and Methods). Figure 3b,c compares the electron–hole liquid model to interlayer photocurrent line traces as a function of increasing power (measured along the dashed line in Fig. 2a). The electron–hole liquid model (Fig. 3b) shows excellent agreement with the photocurrent line profiles, indicating that the interlayer photocurrent is suppressed in the region of the anomalous phase.

Once the critical density $N_C$ is reached, energy added to the electron–hole liquid contributes exclusively to expansion. To see this, we first extract the squared centre-to-edge distance of the photocurrent ring $\ell^2$ from the photocurrent profiles of the photocurrent images shown in Fig. 2a, and plot $\ell^2$ versus power in Fig. 2c. As expected from the linear growth of the 2D volume, $\ell^2$ increases linearly above the critical threshold (purple data in Fig. 2c), exhibiting nearly identical growth to the volume fraction. From the data, we conclude that the state leading to suppressed photoresponse exhibits a well-defined volume that is highly localized, which increases as the number of electron–hole pairs (proportional to the photon fluence) increases. We thus deduce that, similar to a conventional incompressible liquid, the condensate density $N_C$ remains fixed.

The electron–hole liquid phase can be dissociated with a small interlayer voltage. Figure 4a shows spatial photocurrent line cuts as a function of voltage, where the edge of the electron–hole liquid droplet can be tracked via the centre-to-edge distance $\ell$. For interlayer voltages $V_i$ above the built-in potential $\phi_0 = -41$ mV (Supplementary Section 3.1), $\ell^2$ decreases approximately linearly as the voltage increases (Fig. 4b). When the total interlayer voltage exceeds the critical voltage $eV_C = e(V_i - \phi_0) > 45$ meV, electrons and holes become ordinary electron–hole pairs. Above the critical interlayer voltage $V_C$, a spatially uniform photocurrent re-emerges as the 2D liquid dissociates in the electric field.

Although a single pulse with sufficiently high power may form the electron–hole liquid, two-pulse MPDPM measurements reveal the dynamic transition between the electron–hole liquid and gas phase. Figure 5a,b shows the time-resolved photocurrent and photocurrent nonlinearity $\gamma$. When the laser is fixed at the centre of the device, the photocurrent versus $\Delta t$ exhibits a remarkably different power dependence between short and long time delay. At short time delay, the photocurrent at the centre of the device decreases with increasing power above $P_C$ (Supplementary Section 3.2). At long time delay, the photocurrent exhibits ordinary behaviour $I \propto P^{0.52}$ (Fig. 5b). We fit $\gamma$ versus $\Delta t$ to an exponential decay (black line Fig. 5b) to extract the charge density persistence time $\tau = 22$ ps.

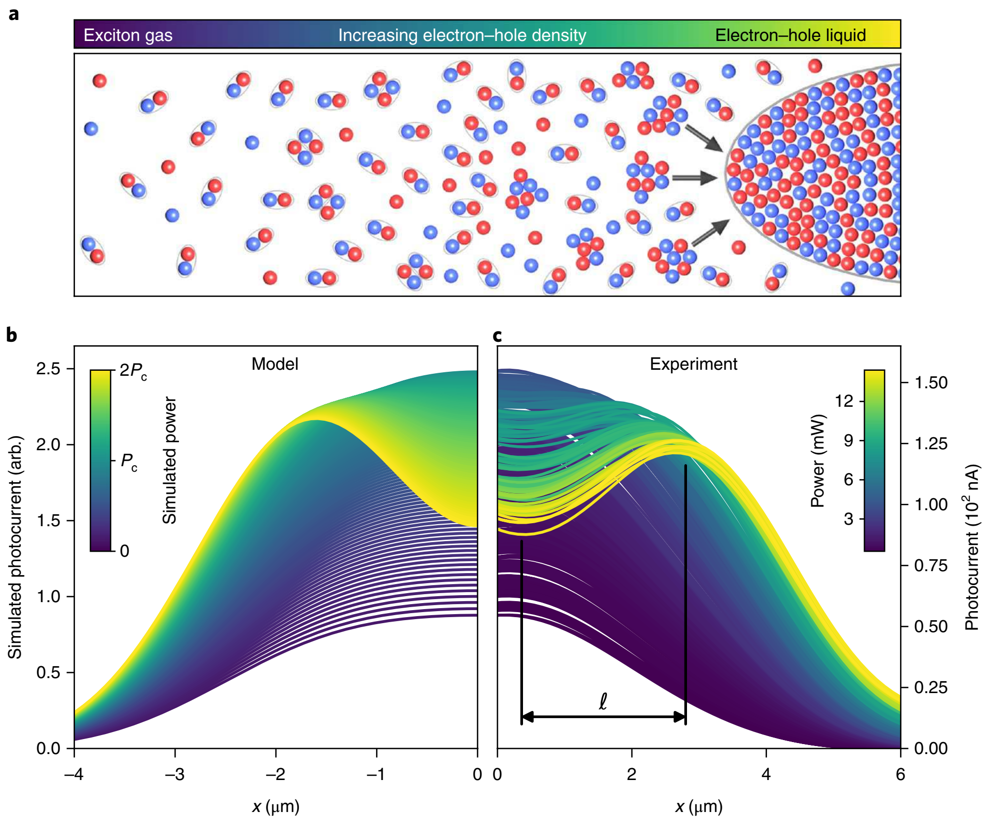

**Fig. 3 | Room-temperature 2D electron–hole liquid and comparison to MPDPM imaging in the MoTe$_2$ photocells. a,** Evolution of electron–hole interactions with increasing electron–hole density. As density increases, the non-interacting gas of excitons gives rise to exciton–exciton interactions, eventually leading to condensation into a 2D electron–hole liquid. **b**, Calculated spatially resolved photoresponse of the electron–hole condensate showing the suppression of photocurrent in the centre of the sample above the critical power $P_C$. **c**, Photocurrent line profiles measured across the centre of the sample for increasing power; $T = 297$ K, $\Delta t = 0.2$ ps.

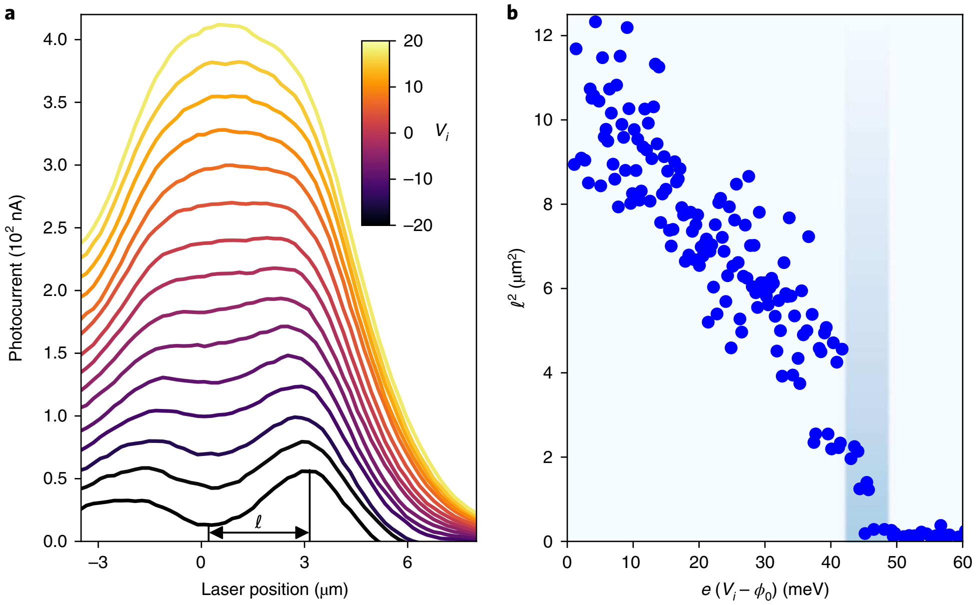

**Fig. 4 | Interlayer voltage dependence of the room-temperature electron–hole liquid. a**, Spatial line cuts of the photocurrent as a function of the interlayer voltage $V_i$; $\Delta t = 0.2$ ps. **b**, Photocurrent ring peak-to-valley distance $\ell^2$ versus interlayer voltage. $\phi_0$ is the built-in potential of the graphene–MoTe$_2$–graphene photocell.

Consistent with observations of the electron–hole liquid in conventional materials, exciton–exciton annihilation precedes the gas-to-liquid phase transition[6,7]. Figure 5c shows the photocurrent versus $\Delta t$ for powers just below and above $P_C$. Below $P_C$ ($P = 3$ mW), the two-pulse photocurrent exhibits excellent agreement with that expected from exciton–exciton annihilation (solid line Fig. 5c)

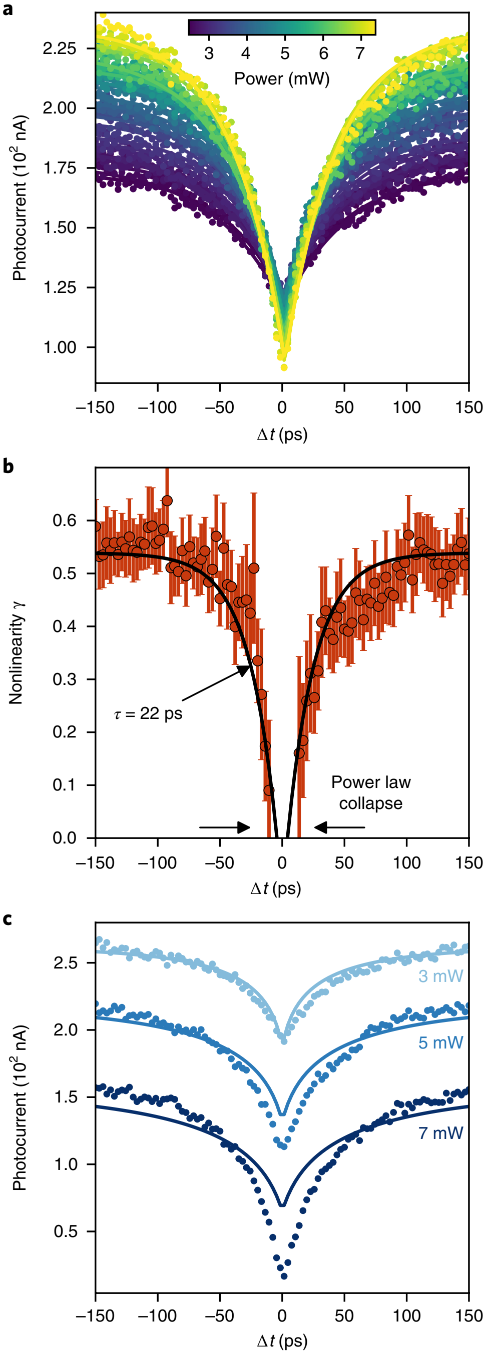

**Fig. 5 | Dynamic photoresponse of the 2D electron–hole liquid.** **a**, Photocurrent versus $\Delta t$ for increasing optical power. The laser is fixed at the centre of the device. Solid lines are exponential fits to the data at each power. **b**, Power law exponent $\gamma$ as a function of $\Delta t$, extracted by fitting the data in **a** to $I \propto P^{\gamma}$. The solid black line is an exponential fit with a characteristic timescale $\tau = 22$ ps. **c**, Photocurrent versus time delay as a function of power, offset for clarity, near the power threshold at 5 mW. Solid lines indicate fits to the exciton–exciton annihilation model that describes the sub-critical photocurrent (Supplementary Section 4).

(Supplementary Section 4.4). At and above $P_C$, when $\Delta t > \tau$ the pulses are independent, and each is insufficient to drive the phase transition. For $\Delta t < \tau$, however, the combined charge density produced by the two pulses is sufficient to form the liquid droplet (see Supplementary Section 5.3). The observed two-pulse photocurrent is then suppressed compared to the photocurrent expected from exciton–exciton annihilation (solid lines Fig. 5c).

In quasi-2D TMDs, the large binding energy and strong Coulomb interactions combine to allow for an exotic electron–hole liquid phase diagram[10], suggesting new device applications that harness electronic fluids at room temperature. The gas-to-liquid phase transition is set by the energy difference $\Delta E$ between the average energy per electron–hole pair in the gas phase and the reduced energy per electron–hole pair in the liquid phase[10] (Supplementary Section 5.3). When $\Delta E$ is large compared to thermal energy at room temperature ($k_B T_{300K} = 26$ meV), the liquid is stable against thermal fluctuations. From the interlayer voltage dependence (Fig. 4a), we estimate that $\Delta E \sim eV_C \sim 45$ meV, approximately twice the thermal energy at room temperature. Although this renormalization is comparable to conventional 2D electron systems, the electron–hole pair binding energy (~$10^2$ meV) in TMDs is several orders of magnitude larger[11,12,29,30]. Such stable collective excitations—potentially exhibiting very high mobility—could have applications in high-power, high-frequency terahertz sources and detectors that can be manipulated with both electronic and optical control.

## Online content

Any methods, additional references, Nature Research reporting summaries, source data, statements of data availability and associated accession codes are available at https://doi.org/10.1038/s41566-019-0349-y.

Received: 29 August 2018; Accepted: 21 December 2018;
Published online: 4 February 2019

## References

1. Lampert, M. Mobile and immobile effective-mass-particle complexes in nonmetallic solids. *Phys. Rev. Lett.* **1**, 450–453 (1958).
2. Kheng, K., Cox, R. & D'Aubigné, M. Observation of negatively charged excitons X$^-$ in semiconductor quantum wells. *Phys. Rev. Lett.* **71**, 1752–1755 (1993).
3. Scholes, G. D. & Rumbles, G. Excitons in nanoscale systems. *Nat. Mater.* **5**, 683–696 (2006).
4. Mak, K. F. et al. Tightly bound trions in monolayer MoS$_2$. *Nat. Mater.* **12**, 207–211 (2013).
5. Keldysh, L. V. *Proceedings of the 9th International Conference on Physics of Semiconductors* 1303 (Nauka, Leningrad, 1968).
6. Jeffries, C. D. Electron–hole condensation in semiconductors. *Science* **189**, 955–964 (1975).
7. Keldysh, L. V. The electron–hole liquid in semiconductors. *Contemp. Phys.* **27**, 395–428 (1986).
8. Kaindl, R. A., Carnahan, M. A., Hägele, D., Lövenich, R. & Chemla, D. S. Ultrafast terahertz probes of transient conducting and insulating phases in an electron–hole gas. *Nature* **423**, 734–738 (2003).
9. Almand-Hunter, A. E. et al. Quantum droplets of electrons and holes. *Nature* **506**, 471–475 (2014).
10. Rustagi, A. & Kemper, A. Theoretical phase diagram for the room-temperature electron–hole liquid in photoexcited quasi-two-dimensional monolayer MoS$_2$. *Nano. Lett.* **18**, 455–459 (2018).
11. Ugeda, M. M. et al. Giant bandgap renormalization and excitonic effects in a monolayer transition metal dichalcogenide semiconductor. *Nat. Mater.* **13**, 1091–1095 (2014).
12. Chernikov, A., Ruppert, C., Hill, H. M., Rigosi, A. F. & Heinz, T. F. Population inversion and giant bandgap renormalization in atomically thin WS$_2$ layers. *Nat. Photon.* **9**, 466–470 (2015).
13. Sun, D. et al. Observation of rapid exciton–exciton annihilation in monolayer molybdenum disulfide. *Nano. Lett.* **14**, 5625–5629 (2014).
14. Froehlicher, G., Lorchat, E. & Berciaud, S. Direct versus indirect band gap emission and exciton–exciton annihilation in atomically thin molybdenum ditelluride MoTe$_2$. *Phys. Rev. B* **94**, 085429 (2016).
15. Zhang, K. et al. Ultrasensitive near-infrared photodetectors based on a graphene–MoTe$_2$–graphene vertical van der Waals heterostructure. *ACS Appl. Mater. Interfaces* **9**, 5392–5398 (2017).
16. Wang, F. et al. Strong electrically tunable MoTe$_2$–graphene van der Waals heterostructures for high-performance electronic and optoelectronic devices. *App. Phys. Lett.* **109**, 193111 (2016).
17. Kuiri, M. et al. Enhancing photoresponsivity using MoTe$_2$–graphene vertical heterostructures. *App. Phys. Lett.* **108**, 063506 (2016).

18. Octon, T. J., Nagareddy, V. K., Russo, S., Craciun, M. F. & Wright, C. D. Fast high-responsivity few-layer $MoTe_2$ photodetectors. *Adv. Opt. Mater.* **4**, 1750–1754 (2016).
19. Ruppert, C., Aslan, O. B. & Heinz, T. F. Optical properties and band gap of single and few-layer $MoTe_2$ crystals. *Nano. Lett.* **14**, 6231–6236 (2014).
20. Lezama, I. G. et al. Indirect-to-direct band gap crossover in few-layer $MoTe_2$. *Nano. Lett.* **15**, 2336–2342 (2015).
21. Kekelidzet, G. P. & Evans, B. L. The photovoltage in single crystals of $\alpha$-$MoTe_2$. *Brit. J. Appl. Phys.* **2**, 855–861 (1969).
22. Gabor, N. M., Zhong, Z., Bosnick, K. & McEuen, P. L. Ultrafast photocurrent measurement of the escape time of electrons and holes from carbon nanotube p−i−n photodiodes. *Phys. Rev. Lett.* **108**, 087404 (2012).
23. Wang, H., Zhang, C., Chan, W., Tiwari, S. & Rana, F. Ultrafast response of monolayer molybdenum disulfide photodetectors. *Nat. Commun.* **6**, 8831 (2015).
24. Ma, Q. et al. Tuning ultrafast electron thermalization pathways in a van der Waals heterostructure. *Nat. Phys.* **12**, 455–459 (2016).
25. Vogt, K. T., Shi, S., Wang, F. & Graham, M. Isolating exciton extraction pathways with electric field-dependent ultrafast photocurrent microscopy. *Conference on Lasers and Electro-Optics* (Optical Society of America Technical Digest, Washington, 2016).
26. Massicotte, M. et al. Picosecond photoresponse in van der Waals heterostructures. *Nat. Nanotechnol.* **11**, 42–46 (2016).
27. Massicotte, M. et al. Photo-thermionic effect in vertical graphene heterostructures. *Nat. Commun.* **7**, 12174 (2016).
28. Sun, Y. et al. The Zeeman splitting of bulk 2H-$MoTe_2$ single crystal in high magnetic field. *Appl. Phys. Lett.* **110**, 102102 (2017).
29. Chernikov, A. et al. Exciton binding energy and nonhydrogenic Rydberg series in monolayer $WS_2$. *Phys. Rev. Lett.* **113**, 076802 (2014).
30. Arora, A. et al. Valley Zeeman splitting and valley polarization of neutral and charged excitons in monolayer $MoTe_2$ at high magnetic fields. *Nano. Lett.* **16**, 3624–3629 (2016).

## Acknowledgements

The authors would like to acknowledge valuable discussions with C. Varma. This work was supported by the Air Force Office of Scientific Research Young Investigator Program (YIP) award number FA9550-16-1-0216, as part of the SHINES Center, an Energy Frontier Research Center funded by the US Department of Energy, Office of Science, Basic Energy Sciences under award number SC0012670, and through support from the National Science Foundation Division of Materials Research CAREER award number 1651247. D.P. and N.M.G received support from SHINES. N.M.G. acknowledges support through a Cottrell Scholar Award, and through the Canadian Institute for Advanced Research (CIFAR) Azrieli Global Scholar Award. T.B.A. acknowledges support from the Fellowships and Internships in Extremely Large Data Sets (FIELDS) Program, a NASA MUREP Institutional Research Opportunity (MIRO) Program, grant number NNX15AP99A. V.A. acknowledges support from the National Science Foundation Division of Materials Research award number 1506707.

## Author contributions

N.M.G. proposed and supervised the project. T.B.A. conducted photoresponse imaging experiments. D.P. synthesized the photocell devices. V.A. supported the direction and interpretation of the experiments through theoretical understanding of the data. All authors participated in analysing the data, interpreting the experimental results and preparing the manuscript.

## Competing interests

The authors declare no competing interests.

## Additional information

**Supplementary information** is available for this paper at https://doi.org/10.1038/s41566-019-0349-y.

**Reprints and permissions information** is available at www.nature.com/reprints.

**Correspondence and requests for materials** should be addressed to N.M.G.

## Methods

**Sample synthesis and characterization.** We obtain bulk graphite from Covalent Materials Corporation and $MoTe_2$ samples from 2D Semiconductors, Inc. Mechanical exfoliation of bulk samples onto $Si/SiO_2$ (290 nm oxide) substrates yields atomically thin flakes of graphene and $MoTe_2$. The heterostructure is constructed using a dry transfer process based on a technique developed by Castellanos-Gomez et al.[31] (Supplementary Section 2.1). This procedure uses a custom-built transfer microscope that picks up the component materials with a polydimethylsiloxane (PDMS)/polypropylene carbonate (PPC) stamp and controllably deposits it on top of another component on a Si substrate. We assemble our heterostructure by picking up and stacking the top graphene onto the $MoTe_2$ flake, then transferring the combined material onto multi-layer graphene. Multi-layer (9 nm) $MoTe_2$ was used to mitigate oxidation during fabrication and avoid complications due to interfacial effects and tunnelling with the graphene. We clean the sample in acetone to ensure removal of the sacrificial PPC layer. We make contact to our heterostructures with standard electron-beam lithography using a Leo SUPRA 55, followed by electron-beam evaporation of 4 nm of Ti and 120 nm of Au using a Temescal BJD 1800. Three devices, all providing similar results, were examined in this work.

Heterostructures are characterized by Raman spectroscopy and atomic force microscopy (AFM) to identify the relative thicknesses of each layer (Supplementary Section 2.2). Raman spectroscopy was performed using a Horiba LabRam in the backscattering configuration with 20 mW of laser power at a wavelength of 532 nm, a 100× objective, and a 1,800 grooves per mm grating. AFM measurements were performed using a Digital Instruments Nanoscope IV with a silicon cantilever in tapping mode to confirm the layer thicknesses of each device.

**Space–time-resolved photocurrent microscopy.** Our optics combine the techniques of scanning beam photocurrent and reflectance microscopy with ultrafast optical pump–probe measurements[32,33] (detailed description in Supplementary Section 1.1). The light source is a MIRA 900 OPO ultrafast pulsed laser which generates 150 fs pulses with controllable wavelengths from 1,150 nm to 1,550 nm at a 75 MHz repetition rate. The OPO is tuned to its peak output at 1,200 nm, close to the A exciton resonance of $MoTe_2$. Due to the spectrally broad nature of ultrafast pulses, approximately 10% of the light is absorbed (Supplementary Section 5.1). The output of the laser is split into two paths by a 50/50 beamsplitter and a translation stage is used to controllably introduce a path length difference, so that a single laser pulse is split into two sub-pulses separated by a time delay $\Delta t$. The recombined beam is then fed into scanning beam optics which consists of rotating mirrors and a system of two lenses that focus the beam onto the back of an objective lens. The objective lens is set at the focal length of the second lens such that, as the scanning mirror rotates, the beam is still focused onto the same position on the back of the objective but arriving at a different angle. The objective lens focuses the light down into a diffraction-limited beam spot where the position of the beam spot depends on the incidence angle. As the scanning mirror rotates, the beam spot moves over a wide range of the sample without aberration, allowing for rapid high-resolution scanning.

To fully enclose our focusing optics inside the vacuum chamber, we use a gradient index of refraction (GRIN) lens as an objective lens. A GRIN lens is a single small cylinder of glass in which the index of refraction is continuously varied along the radial and axial directions. Since it lacks the many interfaces of a conventional objective, a GRIN lens does not disperse the laser pulses as dramatically as a traditional objective lens. We measure a pulse width of approximately 190 fs at the sample. The low pulse dispersion allows us to measure short timescales accurately and gives a high peak intensity.

**Modelling the spatially resolved photoresponse.** To understand the spatial distribution of the photocurrent we need to model what happens when a laser pulse illuminates the sample (Supplementary Section 5.2). At the surface of the sample the laser is a diffraction-limited beam spot with a spatial profile that can be approximated as $P(x) = P_0\exp(-x^2/2\sigma^2)$. Below the critical threshold, $P_C$, the photoresponse obeys a power law $I \propto P^\gamma$. Thus for $P_0 \leq P_{th}$ the observed photocurrent is given by taking the convolution of the Gaussian beam and the photocell profile (working in one dimension for simplicity, but this can easily be generalized to two dimensions):

$$I(x) = \int_{-\infty}^{\infty} P^\gamma(x-x')f(x')\,dx' = \int_{-\infty}^{\infty} P_0^\gamma e^{-\frac{\gamma(x-x')^2}{2\sigma^2}} f(x')\,dx'$$

where $f(x)$ is a function describing the profile of the sample; $f(x) = 1$ on the sample and zero otherwise.

To model the photoresponse in the electron–hole liquid regime we consider the case where, for $P_0 > P_{th}$, an electron hole liquid droplet will form near the centre of the beam spot. Once the droplet forms, it can absorb nearby charge carriers and the electron–hole droplet size should increase linearly as the laser power is increased; thus the size of the droplet $\ell$ is given by $\ell = L_0(P_0 - P_{th})$, where $L_0$ is a free parameter that tunes the rate of expansion of the droplet. Since charge carriers inside the droplet recombine, the part of the beam spot that the droplet is under does not contribute to the observed photocurrent; thus the current is modelled by

$$I(x) = \int_{-\infty}^{-l} P_0^\gamma e^{-\frac{\gamma(x-x')^2}{2\sigma^2}} f(x')\,dx' + \int_{l}^{\infty} P_0^\gamma e^{-\frac{\gamma(x-x')^2}{2\sigma^2}} f(x)\,dx'$$

The observed photocurrent is the convolution of the photocurrent due to gas-phase electron–hole pairs and the photocell active area profile; the volume of the liquid droplet does not contribute to the observed photocurrent, resulting in a suppression of the photocurrent.

## Data availability

The data that support the plots within this paper and other findings of this study are available from the corresponding author upon reasonable request.

## References

31. Castellanos-Gomez, A. et al. Deterministic transfer of two-dimensional materials by all-dry viscoelastic stamping. *2D Mater. Lett.* **1**, 1–8 (2014).
32. Steinmeyer, G. A review of ultrafast optics and optoelectronics. *J. Opt. A* **5**, R1–R15 (2003).
33. Fushitani, M. Applications of pump-probe spectroscopy. *Annu. Rep. Prog. Chem. C* **104**, 272 (2008).